Magnetoplasmonic properties of Ag-Co composite nanohole arrays

Hoang Mai Luong,* Minh Thien Pham, Bin Ai, Tho Duc Nguyen, and Yiping Zhao
Department of Physics and Astronomy, University of Georgia, Athens, Georgia 30602, USA

(Received 14 November 2018; revised manuscript received 7 May 2019; published 10 June 2019)

The magnetoplasmonic properties of Ag-Co composite nanohole arrays are investigated. It is observed that both plasmonic and magnetic properties of the Ag-Co composite nanohole arrays strongly depend on the composition ratio of Ag and Co. The enhanced optical transmission due to plasmonic resonance decreases with the increase of the Co component while the Faraday rotation effect increases monotonically. The magnetization dynamics of a composite thin film is also modified by the composition as well as the introduction of hole arrays. The Ag-Co composite nanohole arrays with the Co content of 30% show high plasmonic–magneto-optics performances compared with that of Ti-Co composite nanohole array, and annealing of the Ag-Co composites in vacuum can further improve this property. All experimental results are confirmed by the finite-difference time-domain calculations. Such a magnetoplasmonic composite material can act as a class of materials for magnetoplasmonic devices or metamaterial applications.

DOI: 10.1103/PhysRevB.99.224413

I. INTRODUCTION

Recently, extensive studies have been accomplished on investigating multifunctional materials and structures with both plasmonic and magnetic properties so their optical properties can be enhanced and controlled by an external magnetic field [1–3]. Such a system has been widely known as a magnetoplasmonic (MOP) system, where magnetic materials (Co, Ni, Fe, garnet, etc.) and noble metals (Ag, Au, etc.) have been often combined [2]. This MOP system has usually been realized via multilayer structures [4–9], which can exhibit enhanced magneto-optics (MO) effects, for instance MO Kerr effect (MOKE) or Faraday rotation (FR), in comparison to identical structures fabricated by pure magnetic material [2,10]. Clearly, an alternative material system that could have both magnetic and plasmonic responses is a composite of noble metals and magnetic materials, such as Ag or Au composites with Co, Ni, or Fe. Transition metals such as Co, Ni, or Fe possess strong magnetic properties at room temperature at a relatively low magnetic field; however, their optical permittivity has a large imaginary part which exhibits a large absorption coefficient, and damps the plasmonic wave [11]. On the other hand, noble metals such as Au or Ag have strong plasmonic effects, but the corresponding MO properties are a few orders of magnitude smaller than that of ferromagnetic materials [2]. Based on the effective medium theory (EMT) [12], the composite of ferromagnetic/plasmonic metal materials [we call composite MOP (CMP) material] could have both plasmonic and magnetic properties, which could open another dimension in the design of MP systems and related devices. Recently, there were only limited experimental works on CMP thin films [11,13–17]. For example, Yang *et al.* studied the composite film of Co and Au with different Co:Au composition ratios and fabrication temperatures, where they noticed that the MO activities increased with increasing Co composition [11]. A recent study by David *et al.* showed an improvement in magneto-optical surface plasmon resonance (MOSPR) responses and signal-to-noise ratio in a MOSPR sensor using a layer of Au-Co alloy instead of a single layer of Au or a trilayer sandwiched Au/Co/Au structure [14]. These studies have attempted to use CMP materials to improve MO performances in different applications. However, they have been focused solely on thin film structures, and the properties of nanostructured CMP materials are generally not considered. Therefore, it would be of great interest to explore the MP properties and potential applications of CMP nanostructures.

In this paper, we investigated the MO performance of Ag-Co CMP nanohole array (CNA) structures. The composition dependent optical transmission, polar MOKE (PMOKE), FR, and Faraday ellipticity (FE) of CNAs in the visible to near-infrared wavelength region were studied. Finite-difference time domain (FDTD) calculations were performed to confirm the experimental results and to give an insight to the relationship between MO properties of CNA structures and their compositions.

II. RESULTS AND DISCUSSIONS

A. Fabrications and characterizations

CNAs were prepared by a combination of the shadowing nanosphere lithography (SNL) method and the codeposition as presented in Fig. 1(a) [18,19]. The polystyrene (PS) nanosphere (diameter D = 500 nm) monolayers were first assembled onto the precleaned glass substrates by an air/water interface method [19–21]. The quality of the PS monolayers was very high, with < 0.8% defect as shown in large zoom-out SEM images of Fig. S1 of Supplemental Material [22]. An oxygen reactive-ion etching was carried out to reduced the size of PS nanospheres to about $d = 350$ nm. The etched PS nanosphere monolayer substrates were loaded into a custom-built dual-source electron deposition system

*hoanglm@uga.edu

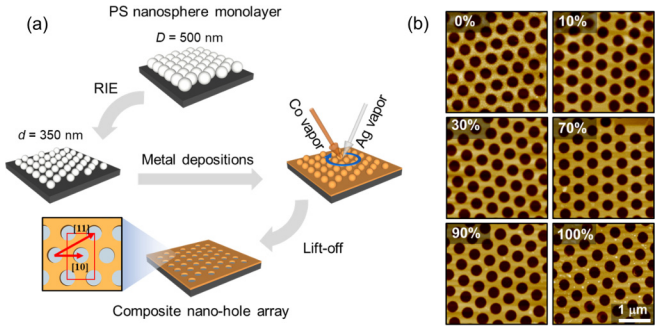

FIG. 1. (a) The fabrication process of the CNAs and (b) representative AFM images of the CNAs with $C_{Co} = 0$, 10, 30, 70, 90, and 100%V, respectively.

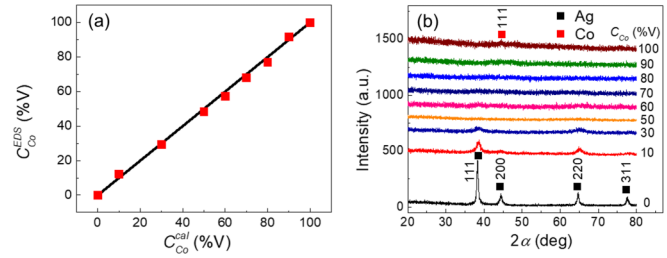

FIG. 2. (a) The plot of C_{Co}^{EDS} (measured by EDS) versus C_{Co}^{cal} (calculated from deposition rates). The ideal case when $C_{Co}^{EDS} = C_{Co}^{cal}$ is presented as a black solid line. (b) XRD profiles of composite thin films for different C_{Co}.

(Pascal Technology) and the vacuum chamber was pumped down under a base pressure of $< 10^{-6}$ Torr. To enhance the adhesion between the glass substrate and composite thin films, a thin layer of Ti (thickness $t_{Ti} = 3$ nm, deposition rate 0.05 nm/s) was first evaporated. Then Ag and Co were deposited simultaneously to form a layer of composite materials. Two crucibles with Ag and Co were placed on two sides of the chamber, and the vapor incident angles to substrate normal were 10° and −10°, respectively. Two separated quartz crystal microbalances were used to monitor the deposition rates and thicknesses of Ag and Co independently. By controlling the deposition rates of Ag and Co, Ag-Co composite thin films with varied volumic composition of Co [$C_{Co} = 0$, 10, 30, 50, 60, 70, 80, 90, and 100 (%V)] were realized. During the codeposition, the substrates were rotated azimuthally with a constant rotation rate of 30 rpm. This constant rotation has been used in previous works to better mix Ag and Co, and allows two components to distribute uniformly through the film thickness [23]. The total thickness of composite film ($t_C = t_{Ag} + t_{Co}$) was kept at 50 nm and the total deposition rate from Ag and Co vapor sources was fixed to be 0.6 nm/s. After the codeposition, PS nanospheres were removed by Scotch tape and the samples were washed subsequently by toluene, isopropyl alcohol, and deionized water, which results in CNA structures as shown in Fig. 1(b). The control samples, the Ag-Co composite thin films with the same thicknesses and compositions, were also fabricated simultaneously on cleaned glass substrates under identical conditions. Before any characterizations, the CNAs and thin film samples were kept inside an MBRAUN glove-box system filled with N_2 (the concentrations of O_2 and H_2O are less than 0.1 ppm) to minimize the potential oxidation effects.

Figure 1(b) shows several representative atomic force microscopy (AFM) images of the hexagonal lattice of nanohole arrays perforated on Ag-Co composite thin films with different C_{Co}. The measured thickness $t_C = 53 \pm 3$ nm and hole diameter $d = 350 \pm 10$ nm (measured at the top surface) (see Fig. S2 in SM) are consistent with the values designed in experiment [22]. Note that the diameter of the hole measured on the top surface is larger than that measured on bottom surface [as seen in Figs. S2(c) and S2(e) in SM [22]], which can be explained by the shadowing effect of the spheres, and the different angles of deposition from the Ag and Co (at ±10°, respectively). Figure 2(a) compares the C_{Co} experimentally determined by energy-dispersive x-ray spectroscopy (EDS) (C_{Co}^{EDS}) with the C_{Co} calculated based on the deposition rates of Ag and Co (C_{Co}^{cal}). The solid line in Fig. 2(a) presents $C_{Co}^{EDS} = C_{Co}^{cal}$. Clearly, in all CMP thin films, C_{Co}^{EDS} and C_{Co}^{cal} are consistently matched with each other, which shows the ability of fully controlled C_{Co} by tuning the relative ratio of Ag and Co deposition rates. Given that C_{Co}^{EDS} is approximately equal to C_{Co}^{cal}, from now on all C_{Co}^{cal} will be referred to as C_{Co} to avoid confusion. Also, CNA samples with a specific Co composition will now be referred to as CNA_x, where $x = 0$, 10, ..., 100, respectively, represents the percentage of Co. In addition, due to the codeposition configuration, both Ag and Co should be mixed uniformly across the entire substrate. For example, a composition mapping of CNA_{50} can be found in Fig. S2 in the SM [22]. From both the top view and cross-section view mapping, both Ag and Co are distributed uniformly.

The x-ray diffraction (XRD) profiles of composite thin films are analyzed and presented in Fig. 2(b). Four prominent peaks can be found at the diffraction angles $2\alpha = 38$, 44, 64, and 78° for the pure Ag thin film ($C_{Co} = 0$%V), which correspond to cubic Ag (111), (200), (220), and (311) planes (JCPDS Ref. No. 01-071-3762), respectively. With the introduction of more and more Co, all these peaks become smaller. Only the Ag (111) and (220) peaks are visible at $C_{Co} < 50$%V, and when $C_{Co} \geqslant 50$%V, they vanish. On the other hand, a very weak peak at $2\alpha = 44°$, which corresponds to the diffraction of fcc Co (111) plane (JCPDS Ref. No. 01-1259), is visible at $C_{Co} = 100$%V. For CMP thin films with $C_{Co} = 50$ to 90%V, no prominent Co peak is observed, which implies that the crystallinity states of Co in these composite films are amorphous (or beyond detection limit).

B. Optical properties of CNAs

Figure 3(a) shows the optical transmission spectra [] of CNAs with different C_{Co}. Several transmission peaks/dips can be identified. The prominent features are two transmission dips **AR1** at $\lambda_1^T \approx 440$ nm and **AR2** at $\lambda_2^T \approx 660$ nm, and one transmission peak **R3** at $\lambda_3^T \approx 850$ nm, which are marked by the dash curves in Fig. 3(a) [and 3(b)]. For CNA_0, the transmission at **R3** (≈ 80%) is significantly larger than the hole coverage (≈ 56%). This enhanced transmission at **R3** is well known as the extraordinary optical transmission (EOT), which has been reported in plasmonic hole lattices made of Ag or Au [24]. At a glance, the magnitude of this EOT peak (**R3**) decreases as C_{Co} increases to 30%V. When

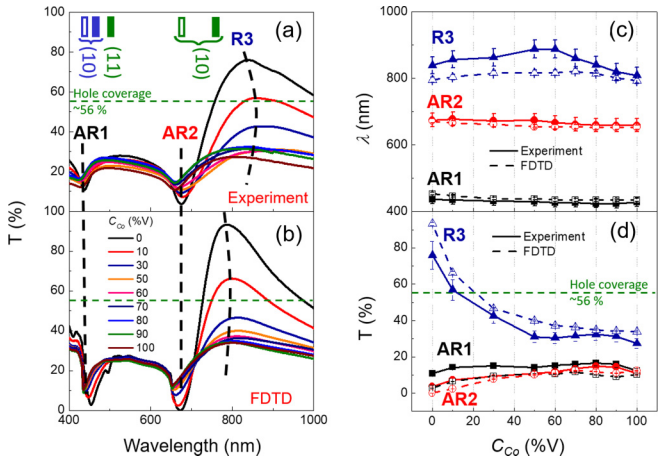

FIG. 3. (a) The experimental and (b) FDTD calculated transmission spectra $T(\%)$ of CNAs. The prominent features of optical transmission (**AR1**, **AR2**, and **R3**) were denoted. The vertical blocks indicate the positions of resonances (solid symbol) and antiresonance (open symbol) at the film-glass interface (green) and film-air interface (blue), calculated from Eqs. (1) and (2). (c) The plots of experimental (solid symbol, solid line) and FDTD calculated (open symbol, dash line) λ_1^T, λ_2^T, and λ_3^T versus C_{Co}. (d) The plots of experimental (solid symbol, solid line) and FDTD calculated (open symbol, dash line) transmission magnitude at **AR1**, **AR2**, and **R3** versus C_{Co}.

$C_{\mathrm{Co}} > 30\%$V, $[T(\%)]$ at **R3** remains almost a constant with C_{Co}. The change in transmission dips **AR1** and **AR2** are less significant. However, a close investigation shows that even the magnitude and position of these three features are changing with C_{Co}, the overall transmission spectra shapes are similar regardless of the composition.

These features result from the coupling effects of light at different material interfaces and surface plasmonic (SP) wave [2,25]. Thanks to the presence of arrays of air hole on the film, it compensates the momentum mismatches of a free-space photon and an SP wave at the metal-dielectric interfaces [26] and produces the transmission resonance or antiresonance at wavelengths λ_{R} and λ_{AR}. For hexagonal crystalline structure, at the transmission peak λ_{R}, the surface plasmon polariton (SPP) Bloch wave condition is satisfied and λ_{AR} can be estimated by the following equation [26,27]:

$$\lambda_{\mathrm{R}} = a_0\left[\frac{4}{3}(i^2+ij+j^2)\right]^{-\frac{1}{2}}\sqrt{\frac{\varepsilon_1\varepsilon_d}{\varepsilon_1+\varepsilon_d}}. \quad (1)$$

At the transmission dip λ_{AR}, the Wood–Rayleigh anomaly condition is satisfied and λ_{AR} can be approximated as [28]

$$\lambda_{\mathrm{AR}} = a_0\left[\tfrac{4}{3}(i^2+ij+j^2)\right]^{-\frac{1}{2}}\sqrt{\varepsilon_d}, \quad (2)$$

where the integers i and j denote the order of the SP resonances, ε_1 and ε_d are the real parts of the dielectric constants of the metal and the dielectric, respectively, and $a_0 = D = 500$ nm is the period of the CNAs. From these equations, the positions of λ_{R} and λ_{AR} were calculated for the case of $\varepsilon_d = 1$ (air) and ε_d of glass, and the results are marked by blocks in Fig. 3(a). The vertical blocks indicate the positions of resonances (solid symbol) and antiresonance (AR) (open symbol) at the film-glass interface (green) and film-air interface (blue). Clearly, the two transmission dips at $\lambda_1^T \approx 440$ nm (**AR1**) and $\lambda_2^T \approx 660$ nm (**AR2**) correspond to the AR (or Wood's anomalies) (1,0) modes of film-air and film-glass interfaces, respectively, while the transmission peak at $\lambda_3^T \approx 850$ nm (**R3**) is the (1,0) resonance mode at film-glass interface. In addition, the local transmission peak between **AR1** and **AR2** could also be assigned as the higher mode resonance (1,1) at film-glass interface.

The FDTD calculated optical transmission spectra of CNAs are shown in Fig. 3(b) and they agree qualitatively well with the experimental results. Three similar distinct features, a transmission peak **R3** and two transmission dips **AR1**, **AR2**, are also found. The EOT peak **R3** is seen as the largest for CNA_0 and it reduces gradually when more Co is added to CNAs. The transmission peak **R3** is observed at $\lambda_3^T \approx 800$ nm, which is slightly blue-shifted in compared to the experimental one. In addition, the two transmission dips AR1 and AR2 are observed at similar wavelengths $\lambda_1^T \approx 440$ nm and $\lambda_2^T \approx 660$ nm in comparison to the features from experimental spectra. For better comparison between experiment and FDTD calculations, the wavelength positions λ_1^T, λ_2^T, and λ_3^T and transmission magnitude $[T(\%)]$ of **AR1**, **AR2**, and **R3** are summarized and plotted in Figs. 3(c) and 3(d). Clearly, λ_1^T and λ_2^T from Figs. 3(a) and 3(b) are overlapped and show the consistency between experiment and FDTD calculation. In addition, λ_1^T and λ_2^T from both experiment and calculation show insignificant changes when C_{Co} increases, which follows well with the Wood–Rayleigh anomaly theory since the Wood's anomalies are purely geometric and the corresponding wavelength position does not depend on the optical permittivity of metal film as stated in Eq. (2) [29]. The EOT wavelength λ_3^T, though it follows a similar trend against C_{Co}, shows larger discrepancy between experiment and FDTD calculation. This can be explained by the fact that λ_3^T has been demonstrated to be dependent on several parameters other than ε_1 as stated in Eq. (1), such as film thickness [30,31], hole diameter [31], hole shape [32], etc., which makes the **R3** peak to be more sensitive to the imperfection of nanostructure than that of **AR1** and **AR2**.

The experimental and FDTD calculated transmission at **AR1**, **AR2**, and **R3** versus C_{Co} shown in Fig. 3(d) also show similar trends. In particular, at the EOT peak **R3**, the transmission rises slowly when C_{Co} decreases from 100%V (pure Co) to 50%V and increases rapidly when C_{Co} decreases from 50%V to 0%V (pure Ag). This shows that when C_{Co} is between 100%V to 50%V, there is negligible EOT effect, and the plasmonic effect occurs only when $C_{\mathrm{Co}} \leqslant 50\%$V. This result agrees with the negligible crystal formation of Ag, observed in Fig. 2(b) when $C_{\mathrm{Co}} \geqslant 50\%$V. On the other hand, at the dips **AR1** and **AR2**, transmissions were observed to be reduced when less Co was added to the composite film. In CNA_{100}, only a weak transmission peak **R3** is induced. This is due to the large absorption of Co film, which can be seen in large imaginary part ε_2 of optical permittivity of Co (from experiment ellipsometry data, Fig. S3 in SM [22]). By adding less Co (i.e., C_{Co} decreases), ε_2 decreases, while the real part ε_1 of optical permittivity becomes more negative and approaches that of the pure Ag, which allows the SPP to propagate a greater length at metal-dielectric interface in comparison to

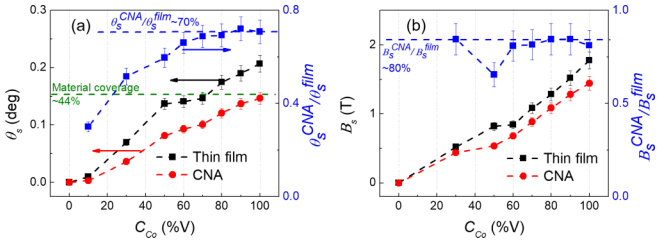

FIG. 4. (a) The plots of the saturated PMOKE (θ_s) and (b) saturation field (B_s) of composite thin film (black) and CNAs (red) for different C_{Co}.

the pure Co case ($C_{Co} = 100\%$V) [33] and eventually boosts up the transmission at **R3**. Therefore, the plasmonic properties of CNAs are improved significantly at low C_{Co}. In addition, stronger plasmonic properties in composite materials also enhance the local electric field at the Wood's anomalies **AR1** and **AR2**, resulting in stronger absorption/deeper dips in transmission spectra. Similar trends can be observed in the FDTD results (dash lines), and the composition-dependent behaviors of transmission at **AR1**, **AR2**, and **R3** agree very well with the experimental results, which show the stronger plasmonic properties when the composite film contains more Ag. Furthermore, the time-averaged local intensity maps of different CNAs at $C_{Co} = 0$, 10, 30, 50, and 100%V at λ_1^T, λ_2^T, and λ_3^T calculated by FDTD have been extracted and are presented in Fig. S4 in SM [22]. In all samples, strong local electrical field at **AR1** and **AR2** can be observed around the rim of the nanoholes at the film-air and film-glass interfaces, respectively, as show in Fig. S4 (**AR1** and **AR2** columns). Figure S4 (**R3** column) illustrates the enhanced asymmetric electric field around the walls and rims of the nanoholes in all the samples at **R3**, which shows that the SP waves at both film-air and film-glass interfaces of the CNAs are coupled and the light from the incident side is re-radiated from other side, which is the origin of EOT [24]. Those observations confirm the prediction of the origins of dips **AR1**, **AR2**, and peaks **R3** as shown in Eqs. (1) and (2). In addition, the ratio of the local electric fields E to the incident field E_0 ($|E/E_0|$) of CNAs for different C_{Co} at the walls of the holes (as indicated by white dotted lines in Fig. S4) are summarized in Fig. S5 in SM. As the C_{Co} in the CNA decreases, the local field ratio at **AR1**, **AR2**, and **R3** increase greatly. This observation confirms our statement about the improved plasmonic properties by the present of more Ag in the CMP nanostructures.

C. Magneto-optical properties of CNAs

Figures S6(a) and S6(b) in SM [22] show the polar MOKE (PMOKE) hysteresis curves (measured at $\lambda = 632$ nm) for the composite thin films and CNAs, respectively (see Sec. XIII in SM [22] for more information, which includes Ref. [34]). For all samples, the hysteresis curves exhibit a typical hard-axis behavior with almost no remanence and saturation fields are at very strong magnetic fields (for instance, at 1.7 T for thin film with $C_{Co} = 100\%$V), which confirms the out-of-plane hard axis of these samples. However, the saturation field (B_s) and saturation PMOKE (θ_s) versus C_{Co} are significantly different for thin film and CNA samples as shown in Figs. 4(a) and 4(b). As presented in Fig. 4(a), for the thin-film sample, the sample with $C_{Co} = 100\%$V produces the largest θ_s, and θ_s drops almost linearly with C_{Co} to null when $C_{Co} = 0\%$V. A similar trend is observed for CNA samples, but θ_s in CNAs is smaller than that in corresponding thin film samples due to the removal of magnetic materials. In principle, θ_s is proportional to ($\propto$) M_s, the saturation magnetization of the samples. In general, $M_s \propto \Theta uA$, where Θ is the coverage of magnetic layer on surface, A is total illuminated surface area of laser beam in MOKE measurement and u is the surface density of magnetic moment, i.e., $\theta_s \propto \Theta$. If we assume that u is the same for thin-film and CNA samples, then $\theta_s^{CNA}/\theta_s^{film} = \Theta_{CNA}$ should be a constant. Figure 4(a) also plots the experimental ratio $\theta_s^{CNA}/\theta_s^{film}$ (blue). Interestingly, even though the materials coverage is only about ~44% for CNAs, the ratio $\theta_s^{CNA}/\theta_s^{film}$ are about 70% for samples with $C_{Co} > 70\%$V. This ratio decreases gradually to 25% for samples with $C_{Co} = 10\%$V. Clearly, the $\theta_s^{CNA}/\theta_s^{film}$ ratio versus C_{Co} is not a constant, which might come from several possible reasons. If we consider a simple Ising model for this composite ferromagnetic/noble metal, the introduction of hole arrays could vary the magnetic interaction at high C_{Co}, which can change the saturation magnetization of CNAs nonlinearly and eventually change θ_s^{CNA} [35]. Another possibility is that the composition changes can modify the surface penetration of the probing laser, which can affect both the θ_s^{CNA} and θ_s^{film}. Further theoretical efforts need to be carried out.

In addition to the saturated PMOKE, the saturation field (B_s) of CNAs and thin films are studied in Fig. 4(b). Basically, B_s is the magnitude of applied magnetic field where the sample is fully magnetized and magnetization is aligned with external magnetic field. We first consider the composition dependencies of these samples. As mentioned before, for pure Co thin film ($C_{Co} = 100\%$V), only a slight remanence can be seen at very strong magnetic field of 1.7 T, due to its out-of-plane hard-axis characteristic. When more Ag is added into the composite materials, the B_s decreases significantly to only about 0.5 T for thin film with $C_{Co} = 30\%$V. This observation implies that the introduction of Ag induces the rise to the out-of-plane components. On the other hand, the introduction of hole arrays also reduces the B_s, as seen in Fig. 4(b) and Fig. S7 in SM [22], where the B_s of CNAs is consistently about 80% of the B_s of composite thin films with the same C_{Co}. This observation is consistent with other work of perforated hole arrays on pure Co thin film [26], and is explained due to the rise of out-of-plane component induced by local dipolar fields which is introduced by the hole edge [26].

As shown above, introducing nanohole arrays and adjusting the composition significantly modifies the magnetic property as well as MO response of composite thin films. To have better understanding about this influence, the composition dependence FR of CNAs has been studied. Figure 5(a) presents the experimental and FDTD calculated FR spectra of CNAs (see Sec. XIII in SM [22] for more information of MO characterizations and FDTD calculations, which includes Refs. [36–40]). In both results, three prominent features can be observed as indicated in Fig. 5(a): a peak **FR1** at $\lambda_1^{FR} \approx 440$ nm, a kink **FR2** at $\lambda_2^{FR} \approx 660$ nm, and a peak **FR3** at $\lambda_3^{FR} \approx 850$ nm. All three features show strong composition

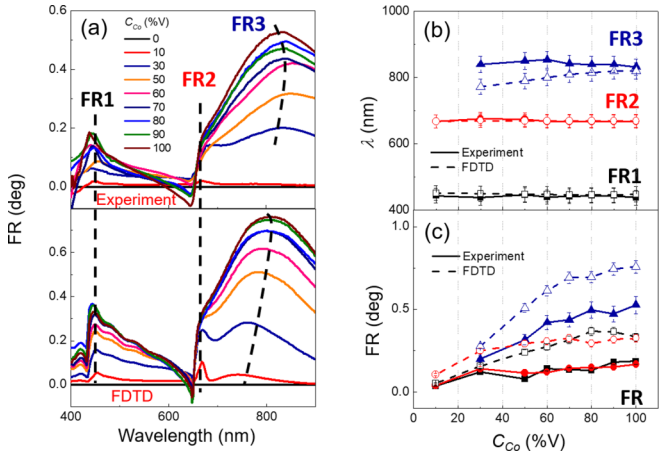

FIG. 5. (a) The experimental and FDTD calculated FR spectra of CNAs. The prominent features of FR (**FR1**, **FR2**, and **FR3**) were indicated. (b) The plots of experimental (solid symbol, solid line) and FDTD calculated (open symbol, dash line) λ_1^{FR}, λ_2^{FR}, and λ_3^{FR} of **FR1**, **FR2**, **FR3** versus C_{Co}. (c) The plots of experimental (solid symbol, solid line) and FDTD calculated (open symbol, dash line) FR at **FR1**, **FR2**, **FR3** versus C_{Co}.

dependence. As C_{Co} decreases, the overall magneto-optical effects of CNAs reduce as seen in the drop of FR magnitude, and the shape of spectra changes significantly. Close to the EOT wavelength λ_3^T, **FR3** is a broad and most distinct FR peak. To better understanding the C_{Co} dependent FR behavior, experimental and FDTD calculated positions and magnitudes of **FR1**, **FR2**, and **FR3** are summarized in Figs. 5(b) and 5(c). The positions of **FR1** and **FR2** are relatively unchanged regardless of the composition of CNAs. In terms of FR magnitude, the composition dependence generally shows an increase of FR when C_{Co} increases in any FR peak [Fig. 5(c)]. When C_{Co} decreases, the location of the **FR3** peak almost remains unchanged but its magnitude decreases significantly. Similar trends can be seen in the **FR1**'s peak positions and magnitude. However, **FR2** shows somewhat different behaviors: at high C_{Co} ($\geqslant$ 50%V), the peak **FR2** is buried in the background and can be considered as a kink in the FR spectra. When $C_{Co} < 50\%$V, **FR2** starts to become a noticeable peak in FR spectra, especially at CNA_{10}. The experimental and FDTD calculated positions of FR features are also in general consistent with each other. However, there still exist some deviations, for example, the positions of **FR3** and the magnitudes of the experimental and FDTD calculated FR. These deviations might come from the fact that the imperfections of experiment structures (such as hole diameter, thickness, roughness of surface, etc.) have not been considered in the FDTD calculation.

Those behaviors of FR features as shown are closely related to the plasmonic behaviors of the CNA samples. Positions of the two features, **FR1** and **FR2**, occur at exact locations of two transmission dips **AR1** ($\lambda_1^T \approx 440$ nm) and **AR2** ($\lambda_2^T \approx 660$ nm), which corresponds to the AR (1,0) mode at the film-air and film-glass interfaces, respectively. Thus it is expected that the origin of these weakly enhanced FR features is from the enhanced electric fields induced by Wood's anomalies at the rims of the nanoholes as well as the long interaction time between light and magnetic layer, which has been demonstrated in an identical structure of Ni and Co nanohole arrays [41,42]. In addition, **FR1** and **FR2** positions are observed to be independent to the C_{Co} [Fig. 5(b)], since **AR1** and **AR2** positions do not depend on the composition of CNAs (as presented in the last section). On the other hand, the magnitude of **FR3** in CNA_{100} is the largest, and its position is coincidentally in the vicinity of **R3**, the EOT peak of CNA_0. Indeed, peak **FR3** is a local FR peak brought by large transmission at the enhanced transmission peak **R3**. Since FR and optical transmittance are indirectly proportionally related [6], the strong transmission peak **R3** at λ_3^T, which is due to SPP resonance (1,0) at Co-glass interface, suppresses the FR magnitude at λ_3^T and creates a local maximum **FR3** at slightly blue-shifted wavelength λ_3^{FR}. The origin of peak **FR3** has been described in more details in our previous work [41].

To isolate the plasmonic effect of Ag on MO properties, FR spectra and $T(\lambda)$ spectra of control samples of Ti-Co CNA samples with $C_{Co} = 80\%$V and 30%V were further investigated. Ti is well known as a poor plasmonic material, and Ti-Co composite control sample can be useful to identify the plasmonic effects from Ag component in Ag-Co samples. The detail of fabrications, measurements, and discussions can be found in Sec. XII in SM [22]. By comparing $T(\lambda)$ and FR spectra of Ti-Co and Ag-Co CNAs, one found that for Ag-Co CNA with low ratio of Ag (i.e., $C_{Co} = 80\%$V), Ag component can raise the plasmonic properties of sample as can be seen in $T(\lambda)$ spectra. However, in this case the amount of Ag in the composite film is not sufficient to create a significantly strong plasmonic effect to enhance magneto-optical properties. On the other hand, for Ag-Co CNA with high ratio of Ag component (i.e., $C_{Co} = 30\%$V), both $T(\lambda)$ at EOT and FR magnitude of Ag-Co CNA are significantly stronger than the ones of Ti-Co CNA samples. This observation implies that by adding more Ag into the CNA sample, stronger plasmonic effects will occur, which might result in enhanced MO effect at high ratio of Ag in composite film.

The influences of C_{Co} and the introduction of nanohole arrays to MO responses are studied further by looking at wavelength-dependent FR of thin-film and CNA samples, and compare the responses at resonant and nonresonant wavelengths. Figure S8 presents FR spectra of composite thin films as a function of C_{Co}. In contrast to CNAs, FRs in all thin-film samples increase monotonically with C_{Co} in the wavelength range $\lambda = 400-900$ nm, and no prominent feature can be found. The composition-dependent FR of thin film and CNAs (normalized for FR of samples with $C_{Co} = 100\%$V) at λ_1^{FR}, λ_2^{FR}, λ_3^{FR} and at a nonresonant wavelength $\lambda_4^{FR} = 750$ nm (denoted by **FR4**) are illustrated in Figs. 6(a)–6(c) and Figs. S9(a)–S9(c), respectively. At a glance, these composition-dependent curves of CNAs at nonresonant wavelength are similar to thin film's curves, though significant differences can be observed at CNA's curves at resonant wavelengths, i.e., at **FR1** and **FR2**. In Figs. 6(a)–6(c), for thin film samples (black curve), a linear relation can be observed regardless of wavelength. However, for CNAs (red curve), there are significant differences between the rise rate of FR when C_{Co} increases from 0%V to 30%V and 50%V to 100%V at **FR1** and **FR2** as seen in Figs. 6(a) and 6(b), respectively. In particular, FR increases rapidly when Ag is still a major

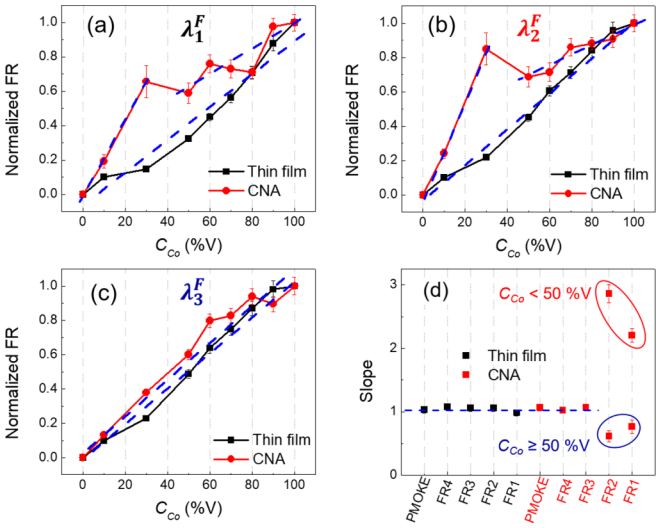

FIG. 6. (a)–(c) Normalized FR of CNAs and composite thin film at λ_1^{FR}, λ_2^{FR}, and λ_3^{FR} versus C_{Co}. (d) The plot of the slopes of normalized FR or PMOKE versus C_{Co}. The dashed curves show linear fitting at different wavelengths.

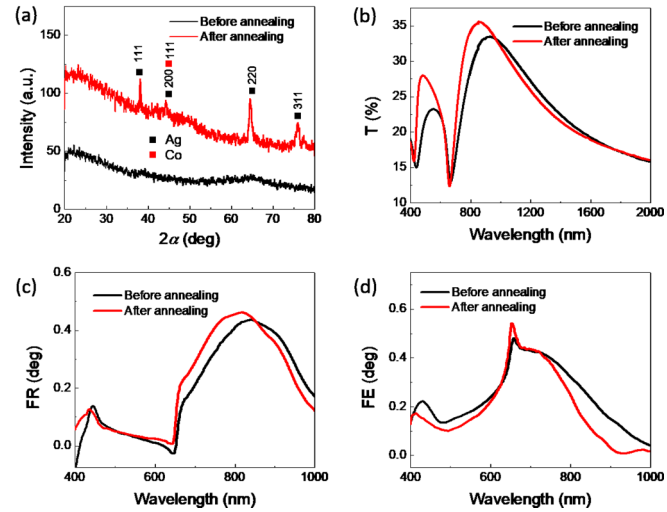

FIG. 7. (a) XRD profile, (b) optical transmission spectra, (c) FR spectra, and (d) FE spectra of CNA_{60} sample before and after annealing.

composition in the film ($C_{Co} = 0$ to 30%V), then increases much slower when $C_{Co} = 50$ to 100%V. On the other hand, at **FR3** of CNAs, we only observe a conventional linear increase of FR against C_{Co} [Fig. 6(c)]. For a better comparison, the normalized FR of CNAs and composite thin film versus C_{Co} at λ_1^{FR}, λ_2^{FR}, λ_3^{FR} and λ_4^{FR} are fitted with a linear function (see Fig. S9 and Table S1 in SM [22]). The slopes of these fittings are summarized in Fig. 6(d). Except **FR1** and **FR2** of CNAs, all other fittings give the slopes ∼1, as expected. However, FRs at the Wood's anomalies, **FR1** and **FR2**, shows much higher slopes (2.21 and 2.86) when $C_{Co} < 50$%V and smaller slopes (0.77 and 0.62 < 1) when $C_{Co} \geqslant 50$%V. This observation can be explained by the enhancement of local electric field due to the plasmonic effect, which comes from high ratio of Ag component in CNAs. Figure S5 shows the magnitude of FDTD calculated local electric field at **AR1** and **AR2**. When $C_{Co} < 50$%V, the plasmonic effect of CNAs is still significantly strong. The FR enhancement due to local electric field adds to the increase of FR due to the amount of magnetic material when C_{Co} increases, and gives a faster rise for FR at Wood's anomalies than that at other nonresonant wavelengths. The difference for **FR1** and **FR2** are due to localized plasmonic effect, while propagation plasmon has less effect. This fast rise was not observed at **FR3**, because the fact that this feature is not raised directly from enhanced electrical field as that of the transmission **R3**, as discussed previously. Nevertheless, when $C_{Co} \geqslant 50$%V, the plasmonic effect does not change as much as seen in Fig. S5(d), therefore the increases of FR in this range come mostly from the increase of magnetic material component in the CMP.

Note that Ag and Co are insoluble in each other in the solid and liquid phases and they cannot rigorously form a binary alloy [11]. Therefore, in this paper, we focus on a mixture rather than an alloy between Ag and Co. Nevertheless, the optical and MO properties of CNA samples can be modified and their MOP effect can be further enhanced by varying a sample's crystallinity, e.g., annealing the sample under high temperature. To demonstrate this point, a representative CNA_{60} sample was annealed in N_2 atmosphere at 500 °C in 2 h. The XRD profile, optical transmission, FR, and FE spectra of the sample before and after the annealing process are summarized in Fig. 7. From Fig. 7(a), while no peak can be found in XRD profile of as-deposited film, several peaks corresponding to crystalline planes of both Ag and Co can be found in the annealed sample, which are caused by the segregation of Ag and Co nanocrystals [11]. The mean crystal sizes of Ag and Co in an annealed CNA_{60} sample extracted from Scherrer's equation are approximately 28 nm and 26 nm, respectively. Due to the changes of the crystallinity and redistribution of Ag and Co in the composite film, the optical and MO properties of CNA are also modified. Figure 7(b) shows the transmission spectra of the annealed sample. Both the (1,0) and (1,1) EOT resonant peaks at the film-glass interface are blue-shifted. This change might come from the relocation of Ag to the film-glass interface. More significantly, the change in plasmonic properties also directly influences FR and FE spectra. As shown in Figs. 7(b) and 7(c), a stronger FR spectrum at **FR3** peak and a stronger and sharper **FE2** peak are observed in the annealed sample. This observation suggests that the crystallinity as well as the redistribution of components also plays an important role in modifying the optical and MO properties of the composite CNA structures. Further systematic experimental efforts need to be carried out for a complete conclusion.

III. CONCLUSIONS

CNAs with different Ag and Co compositions were realized by SNL and electron beam codeposition. Optical properties of CNAs with different C_{Co} has been studied throughout, which shows strong plasmonic properties in samples with high content of Ag. By altering the relative ratio of Ag and Co in the samples, the magnetic and optical properties could be varied, which could be used to improve the MO

performances of CNAs. Our experimental and FDTD calculated results have demonstrated that when $C_{Co} = 30\%V$, a CNA can yield better MO performance than a Ti-Co composite nanohole arrays sample, thanks to the compromise between the strong MO properties from Co component and strong plasmonic properties and large transmission provided by Ag component, or vice versa. Therefore, in addition to the geometrical parameters (size, shape, etc.) and arrangement of the structure, the composition of MOP composite can be adjusted to obtain optimized MO properties. This tunability is promising for the designs and applications of future MOP materials and structures. This also provides new ideas on replacing the multilayers of noble metal/ferromagnetic by composite materials in many current MO devices, such as chiroptical devices, MOSPR sensors, etc., to achieve a better device performance.

ACKNOWLEDGMENTS

This work was supported by National Science Foundation under Grants No. CMMI-1435309 and No. ECCS-1611330 (H.M.L., B.A., Y.Z.) and the University of Georgia (UGA) startup fund and VICOSTONE USA (T.D.N. and M.T.P.).

[1] A. D. B. Ferreira, P. R. Novoa, and A. T. Marques, Composite Structures **151**, 3 (2016).
[2] G. Armelles, A. Cebollada, A. García-Martín, and M. U. González, Adv. Opt. Mater. **1**, 10 (2013).
[3] V. V. Temnov, I. Razdolski, T. Pezeril, D. Makarov, D. Seletskiy, A. Melnikov, and K. A. Nelson, J. Opt. **18**, 093002 (2016).
[4] R. Kekesi, D. Martin-Becerra, D. Meneses-Rodriguez, F. Garcia-Perez, A. Cebollada, and G. Armelles, Opt. Express **23**, 8128 (2015).
[5] V. Belotelov, I. Akimov, M. Pohl, V. Kotov, S. Kasture, A. Vengurlekar, A. V. Gopal, D. Yakovlev, A. Zvezdin, and M. Bayer, Nat. Nanotech. **6**, 370 (2011).
[6] B. Caballero, A. Garcia-Martin, and J. Cuevas, Opt. Express **23**, 22238 (2015).
[7] B. Caballero, A. Garcia-Martin, and J. C. Cuevas, ACS Photonics **3**, 203 (2016).
[8] V. V. Temnov, Nat. Photonics **6**, 728 (2012).
[9] E. Ferreiro-Vila, J. B. Gonzalez-Diaz, R. Fermento, M. U. Gonzalez, A. Garcia-Martin, J. M. Garcia-Martin, A. Cebollada, G. Armelles, D. Meneses-Rodriguez, and E. M. Sandoval, Phys. Rev. B **80**, 125132 (2009).
[10] G. Pellegrini, V. Bonanni, G. Campo, F. Pineider, C. Sangregorio, C. de Julian Fernandez, F. Casoli, M. G. Manera, R. Rella, and G. Mattei, Magnetoplasmonics, in *Encyclopedia of Nanotechnology*, edited by B. Bhushan (Springer Netherlands, Dordrecht, 2015), pp. 1–25.
[11] K. Yang, C. Clavero, J. Skuza, M. Varela, and R. Lukaszew, J. Appl. Phys. **107**, 103924 (2010).
[12] A. Granovsky, M. Kuzmichov, and J. P. Clerk, J. Magn. Soc. Jpn. **23**, 382 (1999).
[13] V. G. Kravets and A. S. Lapchuk, Appl. Opt. **49**, 5013 (2010).
[14] S. David, C. Polonschii, C. Luculescu, M. Gheorghiu, S. Gaspar, and E. Gheorghiu, Biosens. Bioelectron. **63**, 525 (2015).
[15] H. Lu, C. Liu, J. Qin, C. Wang, Y. Zhang, L. Deng, and L. Bi, Photonics Res. **5**, 385 (2017).
[16] S.-Y. Wang, W.-M. Zheng, D.-L. Qian, R.-J. Zhang, Y.-X. Zheng, S.-M. Zhou, Y.-M. Yang, B.-Y. Li, and L.-Y. Chen, J. Appl. Phys. **85**, 5121 (1999).
[17] D. Martin-Becerra, J. M. Garcia-Martin, Y. Huttel, and G. Armelles, J. Appl. Phys. **117**, 053101 (2015).
[18] W. M. Ingram, C. Han, Q. Zhang, and Y. Zhao, J. Phys. Chem. C **119**, 27639 (2015).
[19] S. Larson and Y. Zhao, J. Phys. Chem. C **122**, 7374 (2018).
[20] J. Henzie, J. E. Barton, C. L. Stender, and T. W. Odom, Acc. Chem. Res. **39**, 249 (2006).
[21] B. Ai and Y. Zhao, Nanophotonics **8**(1) (2018), doi: 10.1515/nanoph-2018-0105.
[22] See Supplemental Material at http://link.aps.org/supplemental/10.1103/PhysRevB.99.224413 for experimental details and FDTD calculations; morphology, composition, and MO characterizations of CNAs; and optical and MO properties of Ti-Ag CNAs.
[23] W. Ingram, S. Larson, D. Carlson, and Y. Zhao, Nanotechnology **28**, 015301 (2016).
[24] T. W. Ebbesen, H. J. Lezec, H. Ghaemi, T. Thio, and P. Wolff, Nature **391**, 667 (1998).
[25] T. A. Kelf, Y. Sugawara, R. M. Cole, J. J. Baumberg, M. E. Abdelsalam, S. Cintra, S. Mahajan, A. E. Russell, and P. N. Bartlett, Phys. Rev. B **74**, 245415 (2006).
[26] G. Ctistis, E. Papaioannou, P. Patoka, J. Gutek, P. Fumagalli, and M. Giersig, Nano Lett. **9**, 1 (2008).
[27] H. Raether, *Surface Plasmons on Smooth and Rough Surfaces and on Gratings*, Springer Tracts in Modern Physics (Springer, Berlin, 1988).
[28] D. Maystre, Theory of wood's anomalies, in *Plasmonics*, edited by S. Enoch and N. Bonod (Springer, Berlin, 2012), Vol. 167, pp. 39–83.
[29] A. Hajiaboli, M. Kahrizi, and V.-V. Truong, J. Phys. D **45**, 485105 (2012).
[30] J. H. Kim and P. J. Moyer, Opt. Express **14**, 6595 (2006).
[31] C. Genet and T. Ebbesen, *Nanoscience And Technology: A Collection of Reviews from Nature Journals* (World Scientific, Singapore, 2010), pp. 205–212.
[32] A. Degiron and T. Ebbesen, J. Opt. A: Pure Appl. Opt. **7**, S90 (2005).
[33] S. G. Rodrigo, Extraordinary optical transmission, *Optical Properties of Nanostructured Metallic Systems* (Springer, Berlin, 2012), pp. 37–75.
[34] A. Arora, S. Ghosh, and V. Sugunakar, Rev. Sci. Instrum. **82**, 123903 (2011).
[35] J. V. Selinger, Ising model for ferromagnetism, *Introduction to the Theory of Soft Matter* (Springer, Switzerland, 2016), pp. 7–24.

[36] J. D. Ambekar, R. P. Panmand, R. S. Sonawane, S. K. Apte, D. G. Hundiwale, and B. B. Kale, RSC Adv. **5**, 48112 (2015).
[37] See www.lumerical.com for more detail of Lumerical FDTD solution (2018).
[38] D. Li, L. Chen, C. Lei, J. L. Menendez, C. Mallada, Z. Tang, S. Tang, and Y. Du, JOSA B **33**, 922 (2016).
[39] See www.schott.com for refractive index of N-BK7 glass substrate used in FDTD calculations (2018).
[40] A. K. Zvezdin and V. A. Kotov, *Modern Magnetooptics and Magnetooptical Materials* (CRC Press, London, 1997).
[41] H. M. Luong, B. Ai, Y. Zhao, and T. D. Nguyen, J. Magn. Magn. Mater. **468**, 79 (2018).
[42] M. Rollinger, P. Thielen, E. Melander, E. Ostman, V. Kapaklis, B. Obry, M. Cinchetti, A. Garcia-Martin, M. Aeschlimann, and E. T. Papaioannou, Nano Lett. **16**, 2432 (2016).